Canadian Science Publishing

ARTICLE

Sampling with probability proportional to prediction (3P sampling) using covariates derived from spherical images[1]

Yung-Han Hsu, John A. Kershaw, Jr., Mark J. Ducey, Ting-Ru Yang, and Haozhou Wang

Abstract: Using a two-phase sampling approach with systematic selection of large samples of covariates followed by a sampling with probability proportional to prediction (3P sampling) process to subsample field measures of the parameters of interest can be an efficient design to sample larger forest areas. To assist in obtaining predictions for each sample plot consistently and rapidly, we propose using a 360° spherical camera. In this study, three covariates derived from spherical images were evaluated: (*i*) basal area (P[BA]); (*ii*) sum of squared heights per hectare (P[SHT]); and (*iii*) stem fraction (P[SF]). These covariates were used to estimate volume. Sample simulations showed no biases in volume estimates for any of the three covariates. Overall, P[SF] had the lowest standard error percentages across different simulated sample sizes (10% for five subsamples to 2.5% for 50 subsamples), even though it had the lowest correlations with field volume (correlation = 0.30–0.31). This may be a result of the relatively consistent stand conditions within the study site. Based on our results, standard errors of 5% were obtainable with measurement fractions of about 25% of the number of image-based predictions when using P[SF] or P[BA] and 75% when using P[SHT].

Key words: 3P sampling, spherical image, stem fraction, photo point sampling, vertical point sampling.

Résumé : L'utilisation d'une approche d'échantillonnage en deux phases avec sélection systématique de grands échantillons de covariables, suivie d'un processus d'échantillonnage avec probabilité proportionnelle à la prédiction (échantillonnage 3P) pour sous-échantillonner les mesures sur le terrain des paramètres d'intérêt, peut être une conception efficace pour échantillonner de plus grandes régions forestières. Nous proposons d'utiliser une caméra sphérique à 360°, pour aider à obtenir des prédictions pour chaque parcelle d'échantillonnage de manière cohérente et rapide. Dans cette étude, trois covariables dérivées d'images sphériques ont été évaluées : (*i*) la surface terrière (P[ST]); (*ii*) la somme de la hauteur des tiges au carré à l'hectare (P[SHT]); et (*iii*) la fraction des tiges (P[FT]). Ces covariables ont été utilisées pour estimer le volume. Les simulations d'échantillonnage n'ont montré aucun biais dans l'estimation du volume pour aucune des trois covariables. Dans l'ensemble, P[FT] avait les pourcentages d'erreur-type les plus bas dans les différentes tailles d'échantillon simulées (10 % pour cinq sous-échantillons à 2,5 % pour 50 sous-échantillons), même s'il avait les corrélations les plus faibles avec le volume sur le terrain (correlation = 0,30–0,31). Cela peut être le résultat des conditions de peuplement relativement uniformes dans le site d'étude. Sur la base de nos résultats, des erreurs-types de 5 % ont pu être obtenues avec des intensités de mesure d'environ 25 % du nombre de prédictions basées sur l'image lors de l'utilisation de P[FT] ou P[ST] et de 75 % lors de l'utilisation de P[SHT]. [Traduit par la Rédaction]

Mots-clés : échantillonnage 3P, image sphérique, fraction des tiges, échantillonnage par points photographiques, échantillonnage par points verticaux.

1. Introduction

In practice, forest inventory is designed to obtain estimates of forest conditions under time and cost constraints. Enhancing sampling efficiency is an important consideration in sample design (Freese 1962; Husch 1971; Grosenbaugh 1979; Bitterlich 1984; Iles 2003; Lynch 2017; Yang et al. 2017). Following the sampling principle claimed by Basu (1969), the most efficient sampling design is the one in which the selection probabilities are proportional to the parameters of interest, suggesting that variable probability selection methods should be considered. Variable probability sampling can be employed as a single-phase sampling scheme or as a variant of double sampling (or other forms of hierarchical sampling). Double sampling can be divided into two primary components: (*i*) sample selection criteria and (*ii*) the estimation method. For the sample selection criterion, the original idea was sampling with probability proportional to size (i.e., list sampling). List sampling selects proportional to the sampling unit's contribution to the population (Freese 1962; Cochran 1977; Kershaw et al. 2016); however, it requires a prior census of the entire covariate (large sample) population. Suitable listed covariates in advance of an inventory are usually hard to obtain, so that the application of list sampling is restricted in practice (Furnival et al. 1987). To address this issue, sampling with probability proportional to prediction (3P sampling) was introduced by Grosenbaugh (1965).

The idea of 3P sampling is to establish a selection probability based on a prediction of sampling units. Following the procedure

Received 26 November 2020. Accepted 21 March 2021.

Y.-H. Hsu, J.A. Kershaw, Jr., T.-R. Yang, and H. Wang. Faculty of Forestry and Environment Management, University of New Brunswick, P.O. Box 4400, Fredericton, NB E3B 5A3, Canada.

M.J. Ducey. Department of Natural Resources and the Environment, University of New Hampshire, 114 James Hall, Durham, NH 03824, USA.

Corresponding author: Yung-Han Hsu (email: yhsu@unb.ca).

[1]This article is part of the special issue "Advances in forest mensuration and biometrics, featuring papers presented at the 2020 Western Mensurationists Conference".

from Iles (2003), the parameter of interest or a variable closely related to the parameter of interest for each sampling unit is predicted and compared with a uniform random number drawn from a predetermined range. If the prediction is greater than or equal to the random number, then the sampling unit is selected for detailed measurement (small sample). Because the prediction can be made in the field, there is no need for the census data prior to the sampling process. In fact, the covariate census is completed during the sampling process. When 3P sampling was first developed, it was used to estimate total timber volume of a forest stand and required every tree in a stand to be visited, predictions made, and, if selected for measurement, measured. To apply to larger forest areas, the principle of 3P sampling can be applied using a double sampling context. In this case, the first sample selection phase typically uses a simple random or systematic sample (though any sample design could be used in principle) to select sample points for a large forest area, and then a 3P sampling process is used as the second sample selection phase to select sample points for detailed measurement.

Ratio estimation methods are used to convert (calibrate or "correct") the prediction to the parameter of interest (Freese 1962; Grosenbaugh 1965; Iles 2003; Kershaw et al. 2016). The mean of the ratios between the subsample of measurements and predictions is calculated and used to adjust all predictions. The advantage is that any bias in the predictions can be corrected when the covariate measurements are unbiased, and the precision of the estimate is improved using the two-phase sampling process and the ratio estimate (Grosenbaugh 1965; Iles 2003; Hsu et al. 2020).

Obtaining reliable and repeatable predictions rapidly in the field can make the process more efficient because all sampling units need to be visited and predicted in the 3P sampling process. Traditionally, visual estimates were made (Iles 2003). We propose new methods using a 360° spherical camera to generate the "predictions". Photographic techniques have been used in forest inventory for decades (MacLeod 1919; Andrews 1936; Husch 1947). DeCourt (1956) proposed the use of angle count sampling with terrestrial photographs. Grosenbaugh (1963) developed a detailed treatise on optical dendrometer theory, including applications to photographs. Stewart (2004) applied DeCourt's (1956) ideas to digital photographs and developed distortion corrections for individual photos. Ducey and Kershaw (2011) developed methods for using digital cameras to assist in vertical point sampling. Fastie (2010) and Dick (2012) independently developed methods to estimate stand basal area from 360° horizontal panoramas.

The methods proposed by Fastie (2010) and Dick (2012) required multiple photos acquired in the field and significant postprocessing of the photos in the office to stitch and extract basal area estimates. The postprocessing time may be greater than the time required to obtain the measurements in the field, and the estimates are most likely negatively biased due to occluded (hidden) trees. The relatively new, consumer-grade, 360° spherical cameras offer an alternative digital source that can rapidly record a full view of forest conditions, including the vertical forest structure, in a single image. Rather than extracting complicated tree and stand measurements such as those obtained by Perng et al. (2018), we propose the use of spherical images to obtain easy covariates to be used in a 3P sampling scheme.

The purpose of this study was to evaluate the sampling efficiency of 3P sampling with different image-derived covariates. We combine image-derived covariates with field data collected using fixed-area and big BAF (basal area factor) sampling methods and using a sample simulation process to explore the sampling efficiency and accuracy. Although big BAF sampling was shown to be more cost-effective in practice (Hsu et al. 2020), fixed-area plots may capture different within-field variation, which may influence the correlation with the image-derived covariates. Thus, the effect of the two plot types were explored. Our overall objectives were (*i*) to assess and compare sampling efficiency of 3P sampling using three different covariates derived from spherical images and (*ii*) to explore the effect of plot type (fixed area versus big BAF) on the correlation with these three image-derived covariates and overall sampling efficiency. This study uses existing field data and image-derived covariates to explore the theoretical application of 3P sampling; logistics associated with field implementation require further development and these aspects are discussed.

2. Methods

2.1. Study site and field data

The study area is the 80 ha Femelschlag Research Site located in the Noonan Research Forest (NRF), managed by the University of New Brunswick, Canada (45°59′12′N, 66°25′15′W). Operationally, the NRF is inventoried using big BAF sample plots on a permanent 100 m × 100 m sample grid across the entire forest every 10 years (83 of these sample points were located within the Femelschlag Research Site). The last forest-level inventory was completed in the summer 2012. Following the sampling process mentioned by Marshall et al. (2004) and Kershaw et al. (2016), the big BAF sample plots employed on the NRF used a 2 M BAF angle gauge (i.e., each count tree represents 2 $m^2 \cdot ha^{-1}$ basal area) for selecting count ("in") trees. Species, diameter at breast height (DBH, to the nearest 0.1 cm, breast height = 1.3 m), and status (live or dead) were measured and recorded for all count trees. A 27 M BAF angle gauge was used to select measure trees. Total height (HT, to the nearest 0.1 m) was measured on these trees, and individual tree volume was estimated using the metric volume equations of Honer et al. (1983). The volume to basal area ratio (VBAR) for each measure tree was calculated. Mean VBAR ($\overline{VBAR}$) was estimated from the individual ratios and multiplied by the basal area per hectare ($m^2 \cdot ha^{-1}$) of each sample point to estimate volume ($m^3 \cdot ha^{-1}$).

Within the Femelschlag Research Site, 1/25th ha fixed-area plots (11.28 m radius circular plots) were established on the same 100 m × 100 m sample grid as the big BAF operational inventory. These 83 fixed-area plots were established in 2014. For each tree ≥ 6.0 cm at DBH, species, status (live or dead), DBH, and HT were measured and recorded. As with the big BAF plots, the volume equations of Honer et al. (1983) were used to estimate individual tree volume and volume per hectare ($m^3 \cdot ha^{-1}$) obtained by summing individual tree volume multiplied by the plot expansion factor (25 in this study). The plot-level summaries of the two plot types are given in the University of New Brunswick's DataVerse data archive (Hsu and Kershaw 2020).

In summer 2018, spherical images of the 83 Femelschlag Research Site sample points were obtained using a Ricoh Theta 360° spherical camera (https://theta360.com/en/). The spherical camera was set at 1.6 m above the ground at each sample point. The image height was a constraint resulting from the combination of the minimum height of the height pole and the camera mount. While, ideally, the height would have been the same as breast height (1.3 m), the attributes extracted from the images are used as covariates and are corrected or calibrated by the field data. The covariates do not have to be correct to be useful (Iles 2003, p. 443). Two sample points were disturbed by harvesting activities associated with the Femelschlag study in winter 2016. This makes the field measurements irreconcilable with the image estimates; thus, these two sample points were excluded from this study, leaving 81 sample points for the sampling simulations described below.

2.2. Spherical camera attributes

In this study, three covariates were derived from the spherical images and used as predictors in the 3P sampling process. Ranked (highest to lowest) by amount of time required to extract, the three image-derived covariates were (*i*) stand basal area (P[BA]), approximately 60 s per image, (*ii*) sum of squared heights per hectare

(P[SHT]), approximately 30 s per image, and (*iii*) stem fraction (P[SF]), approximately 10 s per image.

P[BA] was estimated from the spherical images using a modified horizontal point sampling (HPS) process derived from the processes described by DeCourt (1956), Stewart et al. (2004), and Dick (2012). A custom processing program (Wang et al. 2020) was used to obtain tree counts. The spherical images were transformed into cylindrical projections (panoramas), and the trees were counted using a 2 M BAF target along the vertical center of the panoramic image (1.6 m in this case). The number of count trees in each image was multiplied by the BAF to obtain an estimate of P[BA] ($m^2 \cdot ha^{-1}$) for each sample point (for a complete description of the processing program and workflows, see Wang et al. (2020)).

Ducey and Kershaw (2011) showed that estimates of the sum of squared heights from vertical point sampling (VPS) could be an effective covariate in a double sampling framework using vertical digital images. VPS is a variant of sampling with probability proportional to size (Kershaw et al. 2016) introduced by Hirata (1955). In VPS, the radius of the inclusion zone is proportional to tree height, rather than proportional to tree diameter. As a result of the selection geometry, the square of tree height factor (SHF) is the constant factor in VPS:

$$\text{SHF} = \frac{10\,000 \cdot \tan\phi}{\pi} \quad (1)$$

where ϕ is the vertical angle (90° – zenith angle). Maynard et al. (2014) addresses slope correction, which is negligible on moderate slopes. The SHF used in this study was 4520.9 $m^2 \cdot ha^{-1}$ associated with a 50° vertical angle (40° zenith angle). To apply VPS using spherical images, lines were drawn at the 50° parallel (40° zenith angle) on the cylindrical projections (panorama view). Trees taller than the line are counted on each image. The number of count trees was then multiplied by the SHF to yield an estimate of the sum of squared heights (P[SHT]) for each plot.

Stem fraction (P[SF]), defined as the proportion of the image occupied by stem wood, was computed as the stem coverage weighted by zenith angle using a hemispherical projection of the spherical images (Wang 2019). The algorithms for hemispherical image transformation and image pixel classification (stem, foliage, and sky) were developed by Wang (2019). The Beer–Lambert law, a theorical calculation of light transmission through suspended particles (Lambert 1760; Beer 1852), is frequently used to extract canopy structure attributes from hemispherical images (Fournier et al. 2017). Light transmission through the canopy is assumed to be equivalent to light penetrating a medium with randomly distributed particles, and the proportion of light passing is reduced as distance passed through the medium increases (in this case, as the zenith angle increases). In this study, the pixel weight (wt) for different zenith angles (θ) was calculated using a formula adapted from the Beer–Lambert law:

$$\text{wt} = 1 - e^{\left(1 - \frac{\pi}{2 \cdot \theta}\right)} \quad (2)$$

The function gives the highest weight to the pixel at $\theta = 0$ and decreases as θ increases. If the pixel is classified as stem wood, then the weight (wt) for that zenith angle is assigned to that pixel, otherwise 0 is assigned to that pixel. P[SF] is obtained by summing the pixel weights and dividing the sum by the total number of pixels.

2.3. Sample simulation

To test the use of the covariates derived from spherical images as 3P predictors for volume, sample simulation was used. Two key issues were addressed in this paper: (*i*) the efficiency and accuracy of using the three image-derived covariates for volume estimation and (*ii*) the effect of using different plot types. To explore the effects of plot type, sample efficiency based on ratios derived from volume estimates using detailed measurements on fixed-area plots (FAP) were compared with those obtained using big BAF sample points (BBAF).

2.3.1. 3P sample selection

Sample selection in 3P sampling is determined by comparison of predictions with uniform random numbers. As a result, sample size is difficult to regulate precisely, and differences in sample sizes will occur. By controlling the range of random numbers, sample size can be regulated (Grosenbaugh 1965, 1979; Mesavage 1965; Iles 2003). In the original formulation of 3P, the random numbers ranged from 0 to the expected maximum prediction (Grosenbaugh 1965). This approach results in oversampling, and random rejection symbols were introduced to control sample size (Mesavage 1965). Iles (2003) proposed adjusting the maximum random number (KZ) by the inverse of the sampling fraction:

$$\text{KZ} = \frac{K}{P} = K \cdot \left(\frac{N}{n}\right) \quad (3)$$

where K is the expected value (mean) of the prediction, P is the proportion of the population to be selected, N is the population size, and n is the desired sample size. The 3P sampling process was applied at the second phase of double sampling in this study. Thus, N referred to the number of sample points on the systematic grid (81), and n referred to the desired sample size to establish field plots. A larger KZ is equivalent to a larger rejection region, which leads to a smaller sample size.

For each sample size and image-derived covariate, KZ was determined, and the image-derived covariates were used as the prediction in the 3P sampling process. Each of the 81 plots was "visited", a prediction based on one of the three image-derived covariates was obtained, as well as a random uniform number between 0 and the generated KZ. If the image-derived covariate was greater than the random number, then the plot was selected for detailed measurement. The detailed measurement was the volume estimate based on either FAP or BBAF estimates. The desired sample sizes ranged from 5 to 50, in steps of 5. Thus, there were 10 desired sample sizes × 3 image-derived covariates combinations. Each combination was repeated 100 times, and each set was "corrected" using field measurements based on FAP and BBAF estimates.

2.3.2. Ratio estimation in 3P sampling

Data from each plot (i) from each replicate (j) for each simulation scenario (k) were used to estimate the mean ratio and associated sampling errors. For variable probability approaches such as 3P sampling, the mean ratio is typically used:

$$\overline{R}_{jk} = \frac{\sum_{i=1}^{m} \frac{\text{VOL}_{sijk}}{C_{sijk}}}{m} = \frac{\sum_{i=1}^{m} R_{ijk}}{m} \quad (4)$$

where $\overline{R}_{jk}$ is the mean ratio of plot volume to prediction, VOL_{sijk} is the volume of selected plots ($m^3 \cdot ha^{-1}$), C_{sijk} is the image-derived covariate (prediction) of selected plots (e.g., P[BA], P[SHT], and P[SF]), R_{ijk} is the ratio of volume to prediction for selected plots, and m is the number of selected plots. The mean ratio of each replicate (j) for each simulation scenario (k) was then multiplied by the image-derived covariate to convert C to plot volume:

$$\widehat{\text{VOL}}_{ijk} = C_{ijk} \cdot \overline{R}_{jk} \quad (5)$$

where the $\widehat{\text{VOL}}_{ijk}$ is the adjusted volume estimate for the ith sample point, C_{ijk} is the image-derived covariate for the ith sample

point, and $\overline{R}_{jk}$ is the mean ratio. The mean volume estimate for each replicate was then calculated using

$$\overline{\mathrm{VOL}}_{jk} = \frac{\sum_{i=1}^{N} \widehat{\mathrm{VOL}}_{ijk}}{N} \quad (6)$$

where $\overline{\mathrm{VOL}}_{jk}$ is the mean estimated volume for the jth replicate under the kth simulation scenario, and N is the 81 field plots. The sampling error for the estimated volume is a function of the variance of the ratio obtained from the second-phase 3P sample and the first-phase sample variance of the covariate (prediction). In this study, Bruce's formula (Goodman 1960) for percent standard error was used:

$$\mathrm{se\%}(\overline{\mathrm{VOL}}_{jk}) = \sqrt{\left(1 - \frac{m}{N}\right) \cdot \mathrm{se\%}(\overline{R}_{jk})^2 + \mathrm{se\%}(\overline{C}_k)^2} \quad (7)$$

where $\mathrm{se\%}(\overline{\mathrm{VOL}}_{jk})$ is the percent standard error of mean estimated volume; $\mathrm{se\%}(\overline{R}_{jk})$ is the percent standard error of the mean ratio; and $\mathrm{se\%}(\overline{C}_k)$ is the sample standard error of the mean prediction across the first-phase sample. The $(1 - m/N)$ is added as the finite "population" correction to the ratio as the 81 field plots (N) in the first-phase sample represent a relatively small "population" from which the second-phase 3P selections were made (m). Percent standard errors of $\overline{R}_{jk}$ and $\overline{C}_k$ are generally calculated using (Iles 2003):

$$\mathrm{se\%}(\overline{X}) = 100 \cdot \left[\frac{\mathrm{sd}(X)/\sqrt{n}}{\overline{X}}\right] = \left[\frac{\mathrm{CV\%}(X)}{\sqrt{n}}\right] \quad (8)$$

where X is R_{ijk} or C_{ijk}; $\overline{X}$ is the mean of R or C; sd(X) is standard deviation of X; n is sample size; and CV%(X) is the coefficient of variation of X in percent. Although there are more exact formulations to calculate sampling error (Freese 1962; Gregoire and Valentine 2008), Bruce's formula (Goodman 1960; Gove et al. 2020) is an easily accessible formula for most users (Iles 2003) and has been shown to be an efficient estimator of se% in other hierarchical sample designs (Lynch et al. 2021; Budhathoki et al. 2008; Chen et al. 2020; Hsu et al. 2020). This use of Bruce's formula is similar in spirit to the two-phase variance estimator of Rao and Sitter (1995), with the exception that a mean of ratios rather than a ratio of means is employed. To simply verify that Bruce's formula was appropriate, percent standard deviation of $\overline{\mathrm{VOL}}_{jk}$ ($\mathrm{sd\%}(\overline{\mathrm{VOL}}_{jk})$) was calculated as a comparison:

$$\mathrm{sd\%}(\overline{\mathrm{VOL}}_{jk}) = \frac{\mathrm{sd}(\overline{\mathrm{VOL}}_{jk})}{\overline{\overline{\mathrm{VOL}}}_{jk}} \quad (9)$$

where $\overline{\overline{\mathrm{VOL}}}_{jk}$ is the mean of $\overline{\mathrm{VOL}}_{jk}$ across the 100 iterations.

2.4. Data compilation and analysis

To assess the efficiency and accuracy of using the three spherical-image-derived variables as predictors in 3P sampling, bias (observed – predicted) and standard error (eq. 7) were the main criteria used for comparison across the different sample sizes. The bias of mean estimated volume ($\overline{\mathrm{VOL}}_{jk}$) was calculating assuming that the mean volume of 81 field plots was the true value (note that there are two truths: FAP and BBAF):

$$\mathrm{bias} = \overline{\mathrm{VOL}}_F - \overline{\mathrm{VOL}}_{jk} \quad (10)$$

where $\overline{\mathrm{VOL}}_F$ is the mean volume of 81 field plots (from FAP or BBAF).

To simplify and smooth over the multiple sample simulations and to facilitate exploration of sampling efficiency under different image-derived covariates and plot types, a nonlinear mixed-effects model for $\mathrm{se\%}(\overline{\mathrm{VOL}}_{jk})$ and sample size was fitted (Yang et al. 2019; Hsu et al. 2020):

$$\mathrm{se\%}(\overline{\mathrm{VOL}}_{jk}) = \frac{b_0}{m^{b_1}} \quad (11)$$

where m is the number of selected plots (sample size), and the b_i's are the regression coefficients. Random effects were estimated for image-derived covariate type and plot type nested within image-derived covariate type. The combined fixed and random effects can help us understand the influence of both image-derived covariate types and plot types on sampling efficiency. Based on simple random sampling theory, b_0 is the asymptotic maximum se% as the second-phase sample size approaches 0, and b_1 should theoretically equal 0.5. Minimum sample size requirements for 5% standard errors were estimated from the resulting models so that the effects of covariate choice and plot type on sampling efficiency could be more clearly illustrated.

3. Results

3.1. Plot and image-derived covariate summaries

Table 1 shows the field plot summary for the 81 big BAF sample plots (BBAF) and fixed-area plots (FAP). The mean and coefficient of variation (CV) of field-measured volume were 256.8 $m^3 \cdot ha^{-1}$ (25.83%) for BBAF and 271.8 $m^3 \cdot ha^{-1}$ (22.39%) for FAP. Density estimates were 1887 and 1883 stems$\cdot ha^{-1}$ for BBAF and FAP, respectively. Basal area per hectare estimates for BBAF and FAP were 42.0 $m^2 \cdot ha^{-1}$ and 40.0 $m^2 \cdot ha^{-1}$, respectively.

Table 2 summarizes the three image-derived covariates used in this study. P[SF] had the overall lowest se%, while P[SHT] had the highest. Overall, variation within the image-derived covariates was relatively low. The relationships between image-derived covariates and field volumes were generally linear (Fig. 1); however, the correlations were low: around 0.30–0.36 for P[SHT] and P[SF] and up to 0.48 for P[BA] (Table 2). Correlations were similar between plot types but were consistently higher for FAP than BBAF except for the P[BA].

3.2. 3P sampling with spherical-image-derived covariates

Although the correlations with field-measured volume varied among the three image-derived covariates (Table 2), there were no discernible biases in the resulting volume estimates (Fig. 2). Identical to the results for correlation (Table 2), P[SF] typically had narrower ranges of bias followed by P[BA] and then P[SHT]. In terms of bias, no differences between plot types were observed (Fig. 2).

While plot type did not influence bias, it did slightly impact $\mathrm{se\%}(\overline{\mathrm{VOL}}_{jk})$ (Fig. 3). The means of $\mathrm{se\%}(\overline{\mathrm{VOL}}_{jk})$ for FAP were slightly smaller than those for BBAF across all sample sizes (Fig. 3), though the differences decreased as sample size increased (Fig. 3).

The main differences in $\mathrm{se\%}(\overline{\mathrm{VOL}}_{jk})$ were across the three image-derived covariates, which can be influenced by $\mathrm{se\%}(\overline{R}_{jk})$, $\mathrm{se\%}(\overline{C}_k)$, and the correlation between field-measured volume and the image-derived covariates. Although P[SF] had the lowest correlation with field-measured volume (Table 2), the $\mathrm{se\%}(\overline{\mathrm{VOL}}_{jk})$ was the lowest of the three image-derived covariates because of the low $\mathrm{se\%}(\overline{C}_k)$(Fig. 3 and Table 2). While P[BA] had the highest correlation with field-measured volume, it also had relatively high $\mathrm{se\%}(\overline{C}_k)$(Table 2) and, thus, increased $\mathrm{se\%}(\overline{\mathrm{VOL}}_{jk})$. P[SHT], which had both low correlation and high $\mathrm{se\%}(\overline{C}_k)$ (Table 2), had the greatest mean and range of $\mathrm{se\%}(\overline{\mathrm{VOL}}_{\mathrm{jk}})$, making it the least efficient sampling covariate (Fig. 3B). The $\mathrm{sd\%}(\overline{\mathrm{VOL}}_{jk})$ showed a similar trend with $\mathrm{se\%}(\overline{\mathrm{VOL}}_{jk})$ (Fig. 3). Although the $\mathrm{sd\%}(\overline{\mathrm{VOL}}_{jk})$ was slightly higher than the mean of the $\mathrm{se\%}(\overline{\mathrm{VOL}}_{jk})$ in the smaller sample sizes (5 or 10), the differences decreased as sample size increased.

Table 1. Plot-level per hectare means for the 81 sample points by plot type.

	BBAF			FAP		
Parameter	Range (min, max)	Mean	CV, %	Range	Mean	CV, %
Volume ($m^3 \cdot ha^{-1}$)	124.0, 413.5	256.8	25.83	112.1, 432.0	271.8	22.39
Density (stem·ha^{-1})	457, 4233	1887	41.68	575, 4375	1883	43.38
BA ($m^2 \cdot ha^{-1}$)	24.0, 62.0	42.0	22.90	20.9, 53.8	40.0	16.39
QMD (cm)	11.0, 27.0	17.6	19.38	10.5, 26.8	17.3	19.96

Note: BBAF, big BAF sample plot; FAP, fixed-area plot; BA, basal area; QMD, quadratic mean diameter; CV, coefficient of variation. Range is expressed as minimum (min), maximum (max).

Table 2. The range, mean, and se%($\overline{C}$) by sampling covariate and their associated correlation with the field-measured volume by plot type.

				Correlation	
Sampling covariate	Range (min, max)	Mean	se%	BBAF	FAP
P[BA] ($m^2 \cdot ha^{-1}$)	14.0, 56.0	33.4	3.01%	0.478	0.404
P[SHT] ($m^2 \cdot ha^{-1}$)	4520.9, 72334.1	41525.1	4.23%	0.324	0.359
P[SF]	0.231, 0.587	0.448	1.83%	0.310	0.301

Note: BBAF, big BAF sample plot; FAP, fixed-area plot; P[BA], image-derived basal area; P[SHT], image-derived sum of squared heights; P[SF], image-derived stem fraction. Range is expressed as minimum (min), maximum (max).

Fig. 1. Relationships between the three image-derived covariates and the field-measured volumes by plot type: (A) P[BA]–BBAF; (B) P[SHT]–BBAF; (C) P[SF]–BBAF; (D) P[BA]–FAP; (E) P[SHT]–FAP; and (F) P[SF]–FAP (FAP, fixed-area plots; BBAF, big BAF sample plots; P[BA], image-derived basal area; P[SHT], image-derived sum of squared heights; and P[SF], image-derived stem fraction). The black line is the locally weighted regression smoothing line.

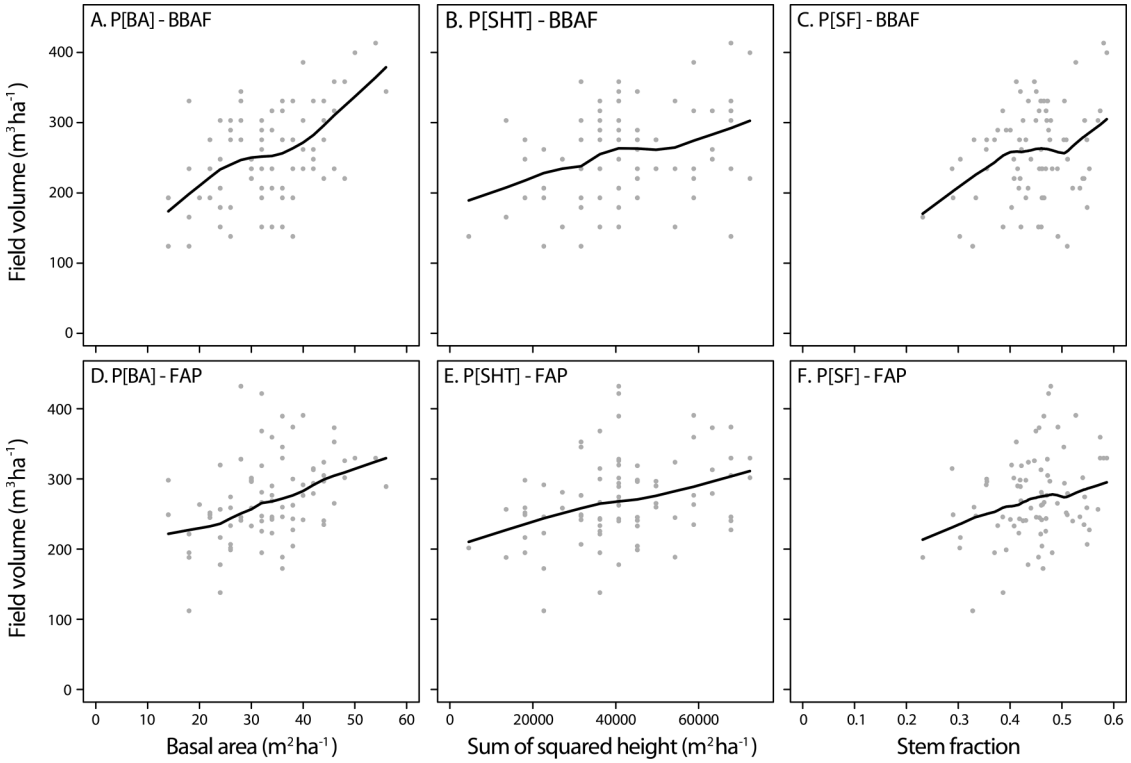

3.3. Sample size estimation

The fixed-effect parameter estimates and their associated standard errors for eq. 11 were $b_0 = 28.220 \pm 3.328$ and $b_1 = 0.479 \pm 0.018$. The standard deviations for the random effects associated with image-derived covariate type were $s(b_0) = 5.718$ and $s(b_1) = 0.029$, and for plot type nested within image-derived covariate type, the standard deviations were $s(b_0) = 0.002$ and $s(b_1) = 0.010$. Table 3 shows the coefficient estimates (fixed + random effects) for eq. 11 by image-derived covariate and plot type. Values for b_1 were around 0.50–0.55 for all combinations (Table 3). Theoretically, these values should be 0.5 based on the standard error calculation under simple random sampling. Higher b_1 coefficients indicate larger reductions in se% with increasing sample size. This result was again consistent with what was observed in Figs. 2 and 3. For all the image-derived covariates, the b_1 coefficients were slightly lower for BBAF than for FAP, indicating the higher variability in BBAF than FAP (Figs. 2 and 3); however, the values for the b_0 coefficient had almost no difference between

Fig. 2. The mean and distribution of bias of $\overline{VOL}_{jk}$ by sampling covariate, plot type, and sample size: (A) P[BA]; (B) P[SHT]; and (C) P[SF] (FAP, fixed-area plot; BBAF, big BAF sample plot; P[BA], image-derived basal area; P[SHT], image-derived sum of squared heights; P[SF], image-derived stem fraction).

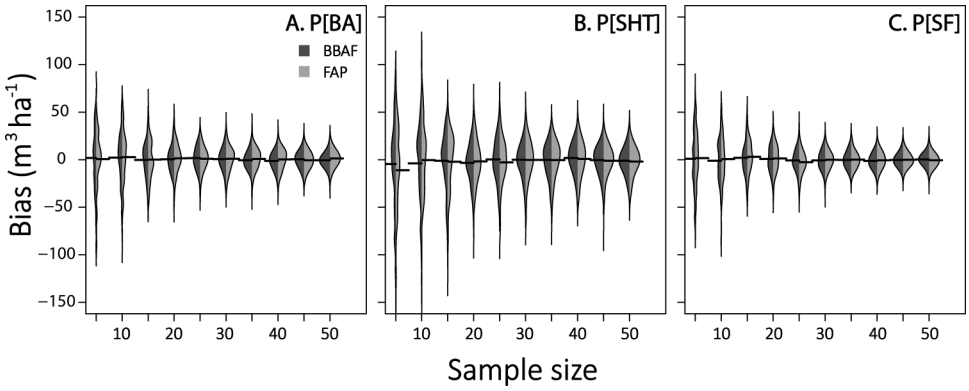

Fig. 3. The sd%($\overline{VOL}_{jk}$) and the mean and distribution of se%($\overline{VOL}_{jk}$) by sampling covariate, plot type, and sample size: (A) P[BA]; (B) P[SHT]; and (C) P[SF] (FAP, fixed-area plot; BBAF, big BAF sample plot; P[BA], image-derived basal area; P[SHT], image-derived sum of squared heights; P[SF], image-derived stem fraction).

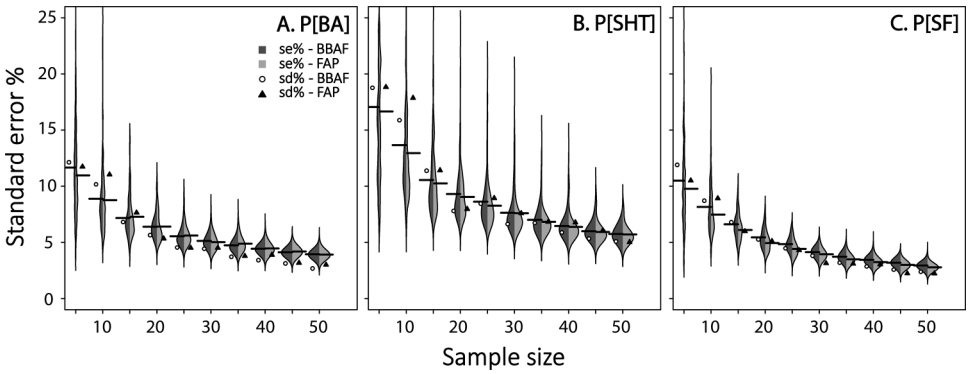

Table 3. Coefficient estimates (fixed + random effects) for the nonlinear mixed-effects model (eq. 11) and the estimated minimum sample size requirements for 5% standard error (se) by plot type and sampling covariate.

	BBAF			FAP		
	Coefficient			Coefficient		
Sampling covariate	b_0	b_1	Sample size for 5% se	b_0	b_1	Sample size for 5% se
P[BA]	24.244	0.454	33	24.244	0.457	32
P[SHT]	36.251	0.457	77	36.250	0.466	71
P[SF]	24.166	0.509	23	24.165	0.530	20

Note: BBAF, big BAF sample plot; FAP, fixed-area plot; P[BA], image-derived basal area; P[SHT], image-derived sum of squared heights; P[SF], image-derived stem fraction.

BBAF and FAP (Table 3). In terms of sample size requirements, standard errors of 5% were obtainable with measurement fractions of about 25% of the number of image-based predictions when using P[SF] or P[BA] and 75% when using P[SHT] (Table 3). BBAF generally required more samples than did FAP, except for P[BA] (Table 3).

4. Discussion

In this study, the resulting se%($\overline{VOL}$) for 3P sampling with the spherical-image-derived covariates (Fig. 3) was largely a function of covariate variation rather than correlation with volume. P[SF] had the lowest correlation with volume and the lowest variability; therefore, the estimates of se%($\overline{VOL}$) using P[SF] as a covariate were lower than the other two image-derived covariates. The low variability in P[SF] resulted in ratios with lower variability. Because se%($\overline{VOL}$) is a function of both se%($\overline{R}$) and se%($\overline{C}$) (eq. 7; Goodman 1960; Gove et al. 2020), in this situation, the major contributor to error, was se%($\overline{C}$), which was fixed and independent of the subsampling procedure (Freese 1962; Iles 2003; Kershaw et al. 2016). Although Bruce's formula (eq. 7; Goodman 1960; Gove et al. 2020) is an approximate calculation for se%($\overline{VOL}$), the minimal differences between sd%($\overline{VOL}$) demonstrated that Bruce's formula gave a reasonable approximate estimate of sampling error.

The power of ratio estimation for bias correction was demonstrated in these results. Ratio estimation can be an effective sampling approach to correct for potential biases and reduce sampling

costs (Freese 1962; Iles 2003; Kershaw et al. 2016; Lam et al. 2018; Hsu et al. 2020). As shown in Fig. 2, the corrected mean $\overline{VOL}$ had no biases across both the different image-derived covariates and different plot types, except at some of the lower sample sizes. Only sample precision was affected by the quality of image-derived covariates. P[BA], which had higher correlations with field-measured volume (Table 2), had a narrower range of biases (Fig. 2).

Based on our sampling efficiency results, P[SF] was the most efficient image-derived covariate; however, this might not be the case in situations with greater variability than what was encountered in this study. The Femelschlag Research Site on the Noonan Research Forest was characterized by relatively uniform stand structures such that the coefficients of variation for volume and DBH were relatively small (Table 1). In this study, se%$(\overline{VOL})$ was impacted more by se%$(\overline{C})$ than by se%$(\overline{R})$, thus favoring P[SF] over the other image-derived covariates. In conditions with more variability in volume, it is expected that P[BA] or P[SHT] might be more highly correlated with volume than P[SF]. In these situations (for example, see Ducey and Kershaw 2011), it is expected that se%$(\overline{R})$ may play a larger role in determining se%$(\overline{VOL})$; in which case, more highly correlated covariates would perform better.

Despite these uncertainties, the use of ratio estimation was very effective and reduced required sample sizes with all image-derived covariates other than P[SHT]. Yang et al. (2019) also showed that variable probability sampling with ratio estimation performed better than with regression estimation and model-derived estimates using Random Forest imputation or nonlinear least squares. The image-derived covariates used here could be used with any selection method in a double sampling or regression sampling framework and produce efficient estimates. While variable probability sampling is theoretically more efficient (Basu 1969), the low correlation observed among the image-derived covariates may not have produced selection probabilities proportional to volume, further contributing to the reduced efficiency. To further improve the correlation, the accuracy of pixel classification would need to be enhanced, or a different weighting function tested.

Currently, the development of our approach would require a field visit to acquire images, postprocessing of images, and a subsequent field visit to measure selected plots. Image processing in the field would be required for a more efficient practical application; however, even given the current limitations, field measurement of the 81 fixed-area plots requires multiple visits over a period of several weeks and, for the big BAF points, multiple visits over several days. Our methods reduced the field effort to approximately 25% of the field plots, so an extra day to acquire images in the field is more than offset by the reduction in field effort required to measure all 81 plots.

In practice, P[SF] was the most automatic image-derived covariate. Both P[BA] and P[SHT] require user interaction to obtain the predictions under the current development of our approach. P[SF], however, is more subject to image quality than the other two measures (Hsu 2019). Sun flecks and shade flecks can impact the accuracy of pixel classifications among stem, foliage, and sky. Simulation results of the impact of fleck intensity on sampling efficiency (Hsu 2019) showed that flecks had very little impact. Again, these results have to be considered within the context of this study and the low variability and low correlations. In situations with higher variability and (or) higher correlations, flecks may play a greater role. Thus, a study with a broader range of conditions is required to better understand the results obtained here. If the correlation between P[SF] and field volume can be enhanced, P[SF] has potential to be an efficient and easily applied image-derived covariate in the field.

Plot type had very little impact on the results in this study. This is similar to the results that Hsu et al. (2020) found for sampling to correct LiDAR enhanced forest inventories. The biggest differences among plot types were the number of trees counted and measured. Subsampling techniques with ratio estimation have consistently been shown to be more efficient in a number of sampling situations (Bell et al. 1983; Corrin 1998; Desmarais 2002; Marshall et al. 2004; Yang et al. 2017; Chen et al. 2019; Hsu et al. 2020). Unless there are other inventory considerations, BBAF is recommended to be used as a sampling method to reduce inventory costs (Yang et al. 2017; Chen et al. 2019), especially for small woodlots (Hsu et al. 2020).

In Yang et al. (2019) and Hsu et al.'s (2020) studies, list sampling with covariates derived from airborne light detection and ranging scanning (ALS) was a better sampling design than 3P sampling. This sampling design requires readily available ALS data. In regions without readily available ALS data, this study shows the potential to apply 3P sampling using covariates derived from a consumer-grade spherical camera. In addition, ALS remains a relatively expensive technology that is likely to only be flown at decadal intervals (Gatziolis and Andersen 2008). The sampling designs developed here could be an efficient and affordable alternative for operational inventories. Although ALS remains a dominant source of landscape-wide auxiliary data in operational work, other technologies are emerging that may provide alternatives. In particular, data from synthetic aperture radar (SAR; Le Toan et al. 1992; Sandberg et al. 2011) or that can enable construction of photogrammetric point clouds (Strunk et al. 2019) are, or will soon be, freely available on frequent intervals over many areas. Photogrammetric point clouds typically provide weaker correlates with forest inventory variables than ALS (Bohlin et al. 2012; Vastaranta et al. 2013; White et al. 2015). The availability of SAR data is not impacted by cloud cover, but relationships with forest biomass can be heavily influenced by soil and canopy moisture and are subject to saturation effects at many wavelengths (e.g., Huang et al. 2018); canopy height models derived from spaceborne SAR are coarse relative to those from operational ALS (Lei et al. 2019). Both sources of data often require preprocessing to yield useful covariates for forest inventory purposes. Nonetheless, evaluation of camera-based techniques in comparison, or in conjunction, with these sources of landscape-level covariates may be fruitful as they move toward operational availability. In addition, spherical images can record ground-based stand conditions in an efficient way. Various tree and stand attributes can be extracted from spherical images and used to estimate important parameters of interest such as biomass and carbon. To make the sampling designs more applicable in the field, development of in-field image processing is required. Image processing to extract covariates in the field using smartphone technology or cloud computing may be an efficient and cost-effective improvement to the sampling designs presented in this study.

Acknowledgements

We are grateful to the dedicated work of the 2012 and 2014 summer field crew (Charles MacPhee, Bonnie Williams, Mike Hutchinson, Shawn Donovan, and Dan Kilham) and the 2018 lab members (Yingbing Chen and Xu Ma) for obtaining spherical images. Funding for this project was provided, in part, by grants from the Natural Sciences and Engineering Research Council of Canada (Discovery Grant program) and the New Brunswick Innovation Foundation Research Assistantship Initiative. M.J. Ducey also gratefully acknowledges the support of the USDA National Institute of Food and Agriculture, McIntire–Stennis Project 1022727 through the New Hampshire Agricultural Experiment Station.

References

Andrews, G.S. 1936. Tree-heights from air photographs by simple parallax measurements. For. Chron. **12**: 152–197. doi:10.5558/tfc12152-2.

Basu, D. 1969. Role of the sufficiency and likelihood principles in sample survey theory. Sankhyā Indian J. Stat. **31**: 441–454.

Beer, A. 1852. Bestimmung der Absorption des rothen Lichts in farbigen Flüssigkeiten [Determination of the absorption of red light in colored liquids]. Ann. Phys. Chem. **86**: 78–88. doi:10.1002/andp.18521620505.

Bell, J.F., Iles, K., and Marshall, D. 1983. Balancing the ratio of tree count-only sample points and VBAR measurements in variable plot sampling. *In* Renewable Resource Inventories for Monitoring Changes and Trends: Proceedings of the International Conference, Corvallis, Ore., 15–19 August 1983. *Edited by* J.F. Bell and T. Atterbury. College of Forestry, Oregon State University, Corvallis, Ore. pp. 699–702.

Bitterlich, W. 1984. The relascope idea: relative measurements in forestry. 1st ed. CAB International, Slough, England.

Bohlin, J., Wallerman, J., and Fransson, J.E.S. 2012. Forest variable estimation using photogrammetric matching of digital aerial images in combination with a high-resolution DEM. Scand. J. For. Res. **27**: 692–699. doi:10.1080/02827581.2012.686625.

Budhathoki, C.B., Lynch, T.B., and Guldin, J.M. 2008. Nonlinear mixed modeling of basal area growth for shortleaf pine. For. Ecol. Manage. **255**: 3440–3446. doi:10.1016/j.foreco.2008.02.035.

Chen, Y., Yang, T.-R.U., Hsu, Y.-H., Kershaw, J.A., and Prest, D. 2019. Application of big BAF sampling for estimating carbon on small woodlots. For. Ecosyst. **6**: 13. doi:10.1186/s40663-019-0172-4.

Chen, Y., Kershaw, J.A., Hsu, Y.-H., and Yang, T.-R. 2020. Carbon estimation using sampling to correct LiDAR-assisted enhanced forest inventory estimates. For. Chron. **96**: 9–19. doi:10.5558/tfc2020-003.

Cochran, W.G. 1977. Sampling techniques. 3rd ed. John Wiley & Sons, New York.

Corrin, D. 1998. BIG BAF: A very efficient sampling method for cruising timber. John Bell and Associates, Corvallis, Ore.

DeCourt, N. 1956. Utilisation de la photographie pour mesurer les surfaces terrières. Rev. For. Fr. **8**: 505–507. doi:10.4267/2042/27219.

Desmarais, K.M. 2002. Using BigBAF sampling in a New England mixedwood forest. John Bell and Associates, Corvallis, Ore.

Dick, A.R.2012. Forest inventory using a camera: Concept, field implementation and instrument development. Unpublished MScF thesis, University of New Brunswick.

Ducey, M.J., and Kershaw, J.A., Jr. 2011. Vertical point sampling with a camera. N. J. Appl. For. **28**: 61–65. doi:10.1093/njaf/28.2.61.

Fastie, C.L. 2010. Estimating stand basal area from forest panoramas. *In* Proceedings of the Fine International Conference on Gigapixel Imaging for Science. Carnegie Mellon University, Pittsburgh, Pa.

Fournier, R.A., Mailly, D., Walter, J.-M.N., and Jonckheere, I.G.C. 2017. Acquiring hemispherical photographs in forest environments: from planning to archiving photographs. *In* Hemispherical Photography in Forest Science: Theory, Methods, Applications. *Edited by* R.A. Fournier and R.J. Hall. Springer Netherlands, Dordrecht. pp. 85–114.

Freese, F. 1962. Elementary forest sampling. Agriculture Handbook No. 232, U.S. Department of Agriculture.

Furnival, G.M., Gregoire, T.G., and Grosenbaugh, L.R. 1987. Adjusted inclusion probabilities with 3P sampling. For. Sci. **33**: 617–631. doi:10.1093/forestscience/33.3.617.

Gatziolis, D., and Andersen, H.-E.R.I.K. 2008. A guide to LIDAR data acquisition and processing for the forests of the Pacific Northwest. Gen. Tech. Rep. PNW-GTR-768. USDA Forest Service, Pacific Northwest Research Station, Portland, Ore.

Goodman, L.A. 1960. On the exact variance of products. J. Am. Stat. Assoc. **55**: 708–713. doi:10.1080/01621459.1960.10483369.

Gove, J.H., Gregoire, T.G., Ducey, M.J., and Lynch, T.B. 2020. A note on the estimation of variance for big BAF sampling. For Ecosyst. **7**: 62. doi:10.1186/s40663-020-00272-x.

Gregoire, T.G., and Valentine, H.T. 2008. Sampling strategies for natural resources and the environment. Chapman Hall/CRC Press.

Grosenbaugh, L.R. 1963. Optical dendrometers for out-of-reach diameters: A conspectus and some new theory. For. Sci. Monogr. **4**: 48. doi:10.1093/forestscience/9.s1.a0001.

Grosenbaugh, L.R. 1965. THREE-PEE SAMPLING THEORY and program "THRP" for computer generation of selection criteriaRes. Paper PSW-RP-21, USDA Forest Service, Pacific Southwest Forest & Range Experiment Station, Berkeley, Calif.

Grosenbaugh, L.R. 1979. 3P sampling theory, examples, and rationale. University of Michigan Library, Ann Arbor, Mich.

Hirata, T. 1955. Height estimation through Bitterlich's method, vertical angle count sampling. Jpn. J. For. **37**: 479–480. doi:10.11519/jjfs1953.37.11_479.

Honer, T.G., Ker, M.F., and Alemdag, I.S. 1983. Metric timber tables for the commercial tree species of central and eastern Canada. Information Report M-X-140. Natural Resources Canada, Canadian Forest Service, Atlantic Forest Centre.

Hsu, Y.-H. 2019. Applications of variable probability sampling using remotely sensed covariates. Master thesis, University of New Brunswick.

Hsu, Y.-H., and Kershaw, J.A., Jr. 2020. Acadian forest volume estimates derived from airborne LiDAR, Big BAF sample plots, and fixed area plots on the Noonan research forest. doi:10.25545/Z8WRBJ.

Hsu, Y.-H., Chen, Y., Yang, T.-R., Kershaw, J.A., Jr., and Ducey, M.J. 2020. Sample strategies for bias correction of regional LiDAR-assisted forest inventory estimates on small woodlots. Ann. For. Sci. **77**: 75. doi:10.1007/s13595-020-00976-8.

Huang, X., Ziniti, B., Torbick, N., and Ducey, M. 2018. Assessment of Forest above Ground Biomass Estimation Using Multi-Temporal C-band Sentinel-1 and Polarimetric L-band PALSAR-2 Data. Remote Sens. **10**: 1424. doi:10.3390/rs10091424.

Husch, B. 1971. Planning a forest inventory. FAO, Rome, Italy.

Husch, B. 1947. A comparison between a ground and aerial photogrammetric method of timber surveying. Unpublished M.Sc. thesis, New York State College of Forestry.

Iles, K. 2003. A sampler of inventory topics. 2nd ed. Kim Iles and Associates, Nanaimo, B.C.

Kershaw, J.A., Jr., Ducey, M.J., Beers, T.W., and Husch, B. 2016. Forest mensuration. 5th ed. Wiley/Blackwell, Hobokin, N.J.

Lam, T., Hsu, Y.-H., Yang, T.-R.U., Kershaw, J.A., and Su, S.-H. 2018. Sampling with probability proportional to prediction: rethinking rapid plant diversity assessment. Forestry, **91**: 17–26. doi:10.1093/forestry/cpx044.

Lambert, J.H. 1760. Photometria sive de mensura et gradibus luminis, colorum et umbrae [Determination of the absorption of red light in colored liquids]. Klett, Augsburg, Germany.

Lei, Y., Siqueira, P., Torbick, N., Ducey, M., Chowdhury, D., and Salas, W. 2019. Generation of large-scale moderate-resolution forest height mosaic with spaceborne repeat-pass SAR interferometry and Lidar. IEEE Trans. Geosci. Remote Sens. **57**: 770–787. doi:10.1109/TGRS.2018.2860590.

Le Toan, T., Beaudoin, A., Riom, J., and Guyon, D. 1992. Relating forest biomass to SAR data. IEEE Trans. Geosci. Remote Sens. **30**: 403–411. doi:10.1109/36.134089.

Lynch, T.B. 2017. Optimal plot size or point sample factor for a fixed total cost using the Fairfield Smith relation of plot size to variance. Forestry, **90**: 211–218. doi:10.1093/forestry/cpw038.

Lynch, T.B., Gove, J.H., Gregoire, T.G., and Ducey, M.J. 2021. An approximate point-based alternative for the estimation of variance under big BAF sampling. For. Ecosyst. **8**: 33. doi:10.21203/rs.3.rs-135016/v1.

MacLeod, M.N. 1919. Mapping from air photographs. Geogr. J. **53**: 382–396. doi:10.2307/1780414.

Marshall, D.D., Iles, K., and Bell, J.F. 2004. Using a large-angle gauge to select trees for measurement in variable plot sampling. Can. J. For. Res. **34**(4): 840–845. doi:10.1139/x03-240.

Maynard, D.S., Ducey, M.J., Congalton, R.G., Kershaw, J., and Hartter, J. 2014. Vertical point sampling with a digital camera: Slope correction and field evaluation. Comput. Electron. Agric. **100**: 131–138. doi:10.1016/j.compag.2013.11.007.

Mesavage, C. 1965. Three-P sampling and dendrometry for better timber estimating. Southern Lumberman, **211**: 107–109.

Perng, B.-H., Lam, T.Y., and Lu, M.-K. 2018. Stereoscopic imaging with spherical panoramas for measuring tree distance and diameter under forest canopies. Forestry, **91**: 662–673. doi:10.1093/forestry/cpy028.

Rao, J.N.K., and Sitter, R.R. 1995. Variance estimation under two-phase sampling with application to imputation for missing data. Biometrika, **82**: 453–460. doi:10.1093/biomet/82.2.453.

Sandberg, G., Ulander, L.M.H., Fransson, J.E.S., Holmgren, J., and Le Toan, T. 2011. L- and P-band backscatter intensity for biomass retrieval in hemiboreal forest. Remote Sens. Environ. **115**: 2874–2886. doi:10.1016/j.rse.2010.03.018.

Stewart, B., Cieszewski, C.J., and Zasada, M. 2004. Use of a camera as an angle-gauge in angle-count sampling. *In* Proceedings of the 2nd International Conference on Forest Measurements and Quantitative Methods and Management, 2004 Southern Mensurationists Meeting. Warnell School of Forestry and Natural Resources, University of Georgia, Athens, Ga. pp. 375–380.

Strunk, J., Packalen, P., Gould, P., Gatziolis, D., Maki, C., Andersen, H.-E., and McGaughey, R.J. 2019. Large area forest yield estimation with pushbroom digital aerial photogrammetry. Forests, **10**: 397. doi:10.3390/f10050397.

Vastaranta, M., Wulder, M.A., White, J.C., Pekkarinen, A., Tuominen, S., and Ginzler, C., et al. 2013. Airborne laser scanning and digital stereo imagery measures of forest structure: comparative results and implications to forest mapping and inventory update. Can. J. Remote Sens. **39**: 382–395. doi:10.5589/m13-046.

Wang, H. 2019. Estimating forest attributes from spherical images. M.Sc. thesis, University of New Brunswick.

Wang, H., Kershaw, J.A., Yang, T.-R., Hsu, Y.H., Ma, X., and Chen, Y. 2020. An integrated system for estimating forest basal area from spherical images. Math. Comput. For. Nat. Res. Sci. **12**: 1–15.

White, J., Stepper, C., Tompalski, P., Coops, N., and Wulder, M. 2015. Comparing ALS and image-based point cloud metrics and modelled forest inventory attributes in a complex coastal forest environment. Forests, **6**: 3704–3732. doi:10.3390/f6103704.

Yang, T.-R., Hsu, Y.-H., Kershaw, J.A, Jr., McGarrigle, E., and Kilham, D. 2017. Big BAF sampling in mixed species forest structures of northeastern North America: influence of count and measure BAF under cost constraints. Forestry, **90**: 649–660. doi:10.1093/forestry/cpx020.

Yang, T.-R.U., Kershaw, J.A., Weiskittel, A.R., Lam, T.Y., and McGarrigle, E. 2019. Influence of sample selection method and estimation technique on sample size requirements for wall-to-wall estimation of volume using airborne LiDAR. Forestry, **92**: 311–323. doi:10.1093/forestry/cpz014.